Front. Struct. Civ. Eng. 2025, 19(4): 541–555
https://doi.org/10.1007/s11709-025-1165-8

RESEARCH ARTICLE

Ground penetrating radar detection of steel fiber reinforced composite linings in shield tunnels: Experimental and field studies

Kang LI[a,b], Xiongyao XIE[a,b*], Hao CHEN[c], Biao ZHOU[a,b], Changfu HUANG[a,b,d]

[a] *College of Civil Engineering, Tongji University, Shanghai 200092, China*
[b] *Innovation Base for Urban Geological Disaster Prevention and Control Technology of the Geological Society of China, Shanghai 200030, China*
[c] *Shanghai Tunnel Engineering Co., (Singapore) Pte. Ltd., Singapore 049712, Singapore*
[d] *China Railway Construction Corporation Limited., Beijing 100855, China*
[*] *Corresponding author. E-mail: xiexiongyao@tongji.edu.cn*

ABSTRACT Steel fiber reinforced concrete-reinforced concrete (SFRC-RC) composite linings are popular in shield tunnel construction due to exceptional strength and waterproofing properties. Non-destructive testing methods are essential for assessing the quality of these linings and ensuring tunnel construction safety. This study investigates the potential and parameters of ground penetrating radar (GPR) detection for the composite linings, using the Deep Tunnel Sewerage System-Phase 2 project in Singapore as a case study. The gprMax simulations incorporated the random distribution and precise parameters of steel fibers to conduct preliminary frequency selection studies. The structural setup of the model experiments mirrored that of the actual tunnel, allowing for an analysis of GPR penetration capabilities at various frequencies. Field testing provided authentic GPR data, validating conclusions drawn from simulations and model experiments and examining GPR power attenuation patterns. Findings indicate that GPR is effective for the quality detection of composite linings. The optimal frequency for detecting SFRC-RC composite linings is 300 MHz, which resolves the interfaces of different layered media. Based on single-parameter exponential and power function fitting, empirical formulas for power attenuation quantitatively characterize GPR signal attenuation in SFRC-RC composite linings. This paper offers valuable references for GPR detection of SFRC-RC composite linings.

KEYWORDS shield tunnel, steel fiber reinforced concrete, composite lining, ground penetrating radar, model experiment, field test

1 Introduction

With the continuous increase in the world's population and the limitations of surface space, the development and utilization of urban underground space have become one of the primary objectives in current underground engineering [1–3]. As a typical form of underground engineering, tunnels play a significant role in various fields such as urban transportation [4–6], including subways [7–9], water supply and drainage [10], energy transmission [11–13], and many others. Due to strict control requirements for surface and building safety and high efficiency during tunnel construction, the shield tunneling method is the mainstream approach for urban underground tunnel construction [14,15]. Timely segment assembly and synchronized grouting during shield tunnel construction can effectively control the of ground loss, manage ground disturbance, and improve the structural integrity of the tunnel itself [16–18]. Traditional shield tunnel linings are mainly composed of precast reinforced concrete (RC) [19], but their crack resistance and water-sealing performance often face challenges in high-water-pressure environments. The steel fiber reinforced

Article history: Received Jul 18, 2024; Accepted Dec 8, 2024

concrete (SFRC) segment, as a novel form of structural support, benefits from an extensive distribution of fibers within, which significantly enhances its crack resistance and impermeability [20–22]. Its utilization in shield tunnel support is experiencing a growing trend. For tunnels with higher impermeability requirements, such as water conveyance tunnels, the adoption of novel multi-layer composite linings including an SFRC layer, RC layer, waterproof layer and grouting layer can endow the lining with superior waterproofing capabilities.

However, due to the invisibility of composite lining materials, the quality of the lining cannot be evaluated through direct visual observation. Traditional core drilling sample methods and impact-echo methods hurt the mechanical properties, suffering from low precision and low efficiency [23]. As a mature, efficient, and highly accurate non-destructive testing technique, ground penetrating radar (GPR) has been widely applied in tunnel lining quality inspection [24–27]. GPR detection of shield tunnel linings has primarily focused on RC structures over the past few decades. In the case of SFRC segments, the presence of steel fibers results in multiple reflections of GPR waves during propagation through the medium, leading to greater interference. Currently, there is limited research on the detection of SFRC segments [28]. conducted numerical simulations and model experiments to study the penetration capability of GPR waves through SFRC segments [29]. investigated the steel fiber density and weak zones in SFRC elements by GPR. However, there is a scarcity of reports on the engineering application of GPR in SFRC segments or composite linings containing SFRC.

This study investigates the feasibility of GPR detection for the steel fiber reinforced concrete-reinforced concrete (SFRC-RC) composite lining of shield tunnel taking the Deep Tunnel Sewerage System (DTSS) Phase 2 in Singapore as an engineering background. Through numerical simulations, model experiments, and field data collection, the optimal GPR detection frequency is determined. The study also examines the waveform characteristics and imaging effects of GPR waves in the multi-layered medium of SFRC-RC composite lining, guiding the parameters of GPR application. Specifically, Section 2 introduces the research background, including the principle differences of GPR detection between SFRC segments and RC segments, the project overview of the DTSS, and the structure of SFRC-RC segments. In Section 3, numerical simulations are conducted for GPR detection of SFRC-RC composite lining. The study focuses on investigating the detection effectiveness of various medium interfaces and defects under different GPR frequencies. Section 4 involves model experiments and field detection conducted within DTSS Phase 2 in Singapore. The study analyzed imaging characteristics at different frequencies and compared and evaluated the detection effectiveness. Sections 5 and 6 present the discussion and conclusions of the paper, respectively.

2 Background

2.1 Differences in ground penetrating radar detection principles for reinforced concrete and steel fiber reinforced concrete layers

The principle of GPR is to use electromagnetic waves to reflect at different material interfaces due to variations in the materials' dielectric constants, which enables the analysis of waveform reflections to obtain information about the detected targets' size, location, and other characteristics. The reflection intensity of electromagnetic waves at material interfaces is determined by the reflection coefficient shown in Eq. (1) [30]. The greater the difference in ε_1 between ε_2, the stronger the reflection intensity of the GPR waves at that interface, leading to a more pronounced corresponding reflection waveform.

$$C_{\mathrm{r}} = \left| \frac{\sqrt{\varepsilon_1} - \sqrt{\varepsilon_2}}{\sqrt{\varepsilon_1} + \sqrt{\varepsilon_2}} \right|, \tag{1}$$

where ε_1 and ε_2 represent the relative dielectric constants of the two materials.

As shown in Fig. 1, there are certain differences in the detection of GPR in RC and SFRC segments. For RC segments, the incident electromagnetic waves generated by the GPR transmitting antenna T_x will undergo reflections at the interfaces of the segment's edges and rebars. As rebars are strong reflectors, multiple

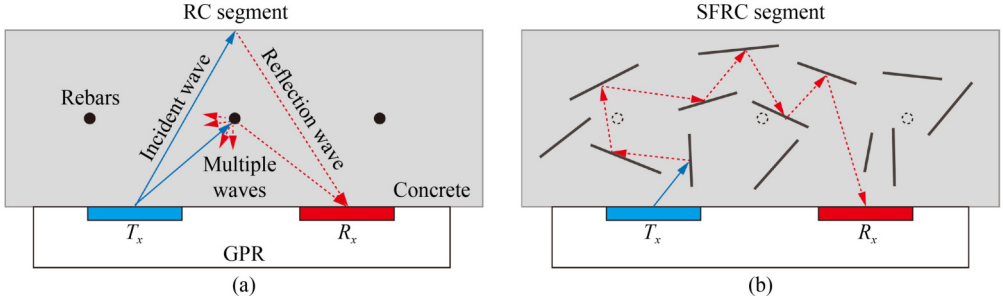

Fig. 1 The Difference in GPR detection principles between (a) RC segment and (b) SFRC segment.

reflections occur around them, resulting in strong multiple waves. These interfaces and multiple waves will be detected by the receiving antenna R_x. Unlike RC segments, SFRC segments incorporate a significant concentration of internal steel fibers, resulting in a more intricate reflection path for electromagnetic waves within the SFRC segments, as illustrated in Fig. 1(b). As a result, the reflected waveforms captured by the receiving antenna contain more interference.

2.2 Structure of the steel fiber reinforced concrete-reinforced concrete composite lining

As shown in Fig. 2(a), the novel multi-layer composite lining mainly consists of three parts from the outside: primary lining predominantly made of RC, secondary lining made of SFRC and high-density Polyethylene (HDPE) [31] waterproof layer. The thickness of these three layers is 200, 225, and 2.5 mm, respectively. Simultaneously, to compensate for the shield tai gap caused by cutter over-excavation, it is necessary to carry out synchronous grouting during the construction process to improve the lining's stress distribution and compensate for ground losses.

As shown in Fig. 2(b), different interfaces of the composite lining are labeled with different numbers for ease of distinction. Here, I represents the interface between free space and the HDPE layer, II represents the interface between the SFRC layer and the RC layer, III represents the interface between the RC layer and the grouting layers, IV represents the interface between the grouting layer and the geological stratum. Due to the relatively small thickness of the HDPE layer and its minimal interference with electromagnetic waves, it is not considered a detection target in the GPR research and it is not numbered among the interfaces with the SFRC layer.

The parameters and content of steel fibers in the composite lining have a significant impact on GPR detection performance, but their specific values are determined by the strength requirements of the lining in the particular project, which may vary between different projects [32]. The parameters of the steel fibers in SFRC layers of Phase 2 of DTSS are displayed in Table 1. The dosage of the steel fibers in the SFRC layer is 40 kg/m^3, which can be converted to a content of ω = 0.513%. The density of a single steel fiber is 7.8 g/cm^3, donated as ρ_0. The diameter D and length L are 0.75 and 60 mm, respectively.

2.3 Research approach

The research approach of this paper is illustrated in Fig. 3. Three main research methods, namely numerical simulation, model testing, and field testing, are employed to investigate the feasibility and application of GPR on the SFRC-RC composite lining of shield tunnels. The proles of the three research methods are as follows.

1) Numerical simulation provides initial comparative options and guidance for the frequency selection of GPR in detecting SFRC-RC composite lining.

2) After the preliminary frequency range is determined, model testing is employed to assess the penetration performance of GPR waves in SFRC-RC composite lining within the selected frequency range.

3) Field GPR testing is conducted within a localized section of DTSS Phase 2. The optimal GPR detection frequency for the SFRC-RC composite lining is determined based on the analysis of collected GPR data's waveform characteristics (A-scan), imaging features (B-scan), and power attenuation characteristics. Simultaneously, this process validates the results obtained from numerical simulation and model experimentation.

The three methods possess a characteristic progression from simplicity to complexity, from ideality to reality in terms of working conditions. They investigate the detection effectiveness of the SFRC-RC composite lining in shield tunnels from different perspectives, which enhances the persuasiveness and credibility of the research outcomes.

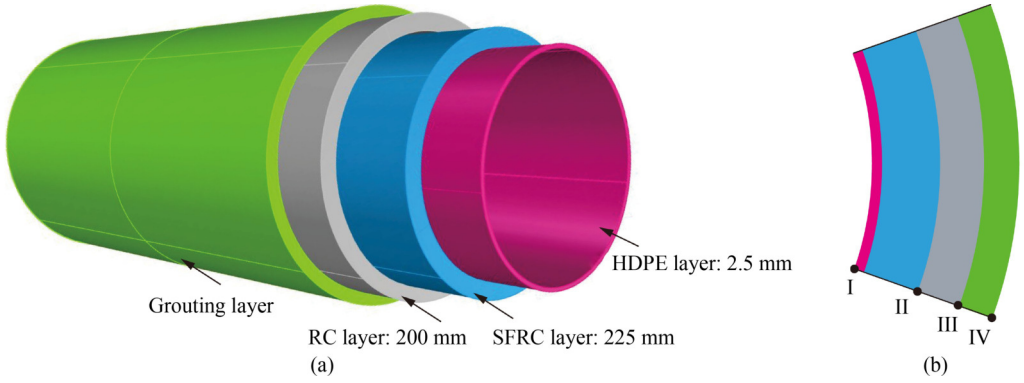

Fig. 2 The novel composite lining consisting of HDPE layer, SFRC layer, RC lining and grouting layer: (a) the structure; (b) the illustration of interface numbering for the media boundaries.

3 Numerical simulations for the composite lining detection

3.1 Finite Difference Time Domain (FDTD) method and gprMax

The propagation of electromagnetic waves in a medium is governed by Maxwell's equations as shown in Eq. (2) [33]. The key challenge in numerical simulations for GPR is to solve the equations in complex media.

$$\begin{cases} \nabla \times H = \sigma E + \varepsilon \dfrac{\partial E}{\partial t}, \\ \nabla \times E = -\mu \dfrac{\partial H}{\partial t}, \\ \nabla \cdot E = 0, \\ \nabla \cdot H = 0, \end{cases} \tag{2}$$

where E and H are the electric field intensity and the magnetic field intensity, respectively. ε and μ represent the relative dielectric constant and relative magnetic permeability of the medium, respectively.

gprMax 3.0 is an open-access numerical software widely utilized for GPR simulations [34–37]. Its principle is to solve Maxwell's equations in three-dimensional (3D) using FDTD [38]. The Yee's algorithms are utilized to discretize the spatial 3D medium into Yee cells, as illustrated in Fig. 4. As can be seen from the figure, the magnetic field H and electric field E are spatially interleaved in the Yee cells, and each spatial component is well-suited for solving Maxwell's equations using the finite difference method.

The main drawback of FDTD is its low computational efficiency. To improve computational efficiency in this paper, a 2D numerical model is employed, which involves the construction of a multi-layered composite lining.

Table 1 The primary parameters of steel fiber in the SFRC segment

Parameter	Value
ρ_0 (g·cm^{-3})	7.8
L (mm)	60
D (mm)	0.75

3.2 Setup of the numerical model

3.2.1 Modeling method for steel fiber reinforced concrete layer

The numerical model of the SFRC layer needs to consider the random distribution and actual dimensions of the steel fibers. The generation process and principle of steel fibers are presented in Figs. 5(a) and 5(b), respectively. The quantity of steel fibers is calculated using Eq. (3), where both the area ratio and content are taken into consideration. After determining the number of steel fibers, random starting coordinates (x_0, y_0) for the steel fibers are generated within the SFRC layer. Subsequently, the endpoint coordinates (x_n, y_n) are calculated using Eq. (4), where the fixed distance L is maintained, but the distribution angle α is randomized. Steel fibers continue to be generated until reaching a total of n, and the portion beyond the SFRC range is removed, resulting in the SFRC layer.

In gprMax, the steel fiber model is established using the built-in "cylinder" component. This involves generating random cylinders within the model, with (x_0, y_0) as the starting point and (x_n, y_n) as the endpoint, and having a diameter of D.

$$n = \frac{\omega V}{V_0} = \frac{\omega S}{S_0}, \tag{3}$$

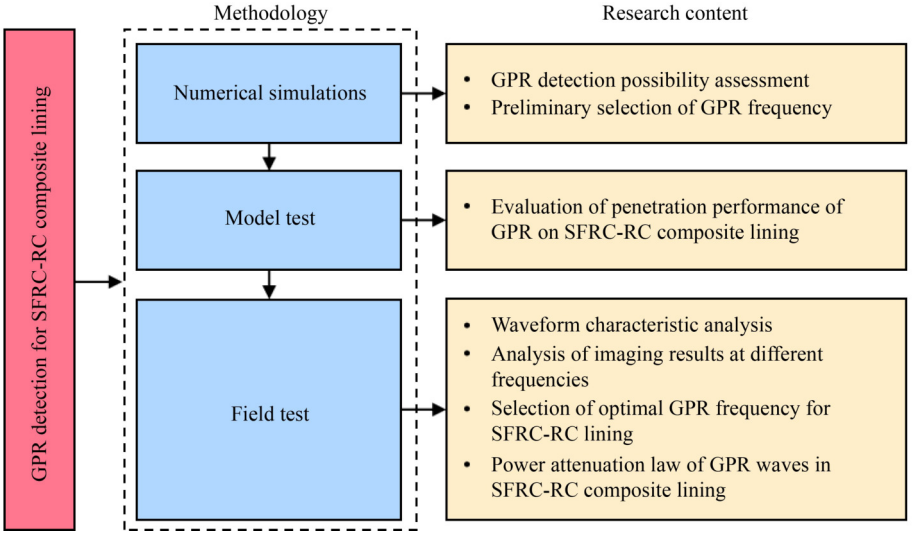

Fig. 3 Research routes of the GPR detection for SFRC-RC composite lining.

where n is the number of steel fibers in the numerical model; V is the volume of the SFRC layer; V_0 is the volume of a single steel fiber; when the numerical model was in two-dimensional, the V and V_0 are replaced by corresponding area values S and S_0, respectively.

$$(x_n, y_n) = (x_0 + L\cos\alpha, y_0 + L\sin\alpha), \tag{4}$$

where (x_0, y_0) represents the starting point of the steel fibers numerical model; (x_n, y_n) represents the ending point of the steel fibers; α is the inclination angle of the steel fibers.

3.2.2 Characteristics of the numerical model

3.2.2.1 Model dimensions and boundary conditions

The gprMax numerical model, as shown in Fig. 6, has a length of 1 m, and a height is 0.65 m. To achieve detailed modeling of a large number of randomly distributed steel fibers, the minimum mesh size is set to 0.0005 m. The thickness of the HDPE layer, SFRC layer, and RC layer in the model is 2.5 mm, 0.225 m, and 0.2 m, respectively. The Perfectly Matched Layer [39] was used as the boundary absorbing condition in numerical simulations to avoid the reflection of GPR waves at the model boundary, with a thickness of 10 times the minimum grid size of the model.

For the distribution of reinforcing mesh in tunnel linings, different simplification methods are usually adopted when simulating with gprMax. For example, some researchers simplify the mesh by modeling a few rebar elements [40,41], while others use isotropic media with equivalent dielectric constants [42]. This study adopts the latter simplification method for the following three reasons. 1) This study does not focus on the propagation laws and characteristics of electromagnetic waves within RC layers, but instead aims to simulate the overall behavior of electromagnetic wave penetration through the medium. Therefore, from the results perspective, this simplification is acceptable. 2) The distribution of the rebar mesh in the RC layer is complex, making it difficult for the gprMax software to create a model that perfectly replicates the actual engineering scenario. Even if a simplified rebar model is established, the imaging results would differ significantly from the actual outcomes. 3) The distribution of the rebar mesh in the RC layer is relatively uniform; therefore, the composite structure formed by the rebar mesh and concrete can be simplified to a homogeneous medium with an equivalent relative permittivity.

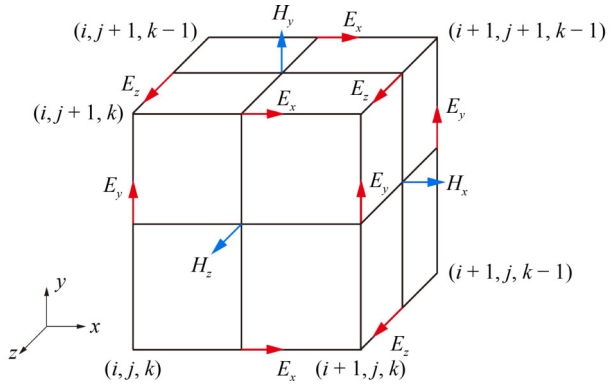

Fig. 4 Structure of Yee's cell.

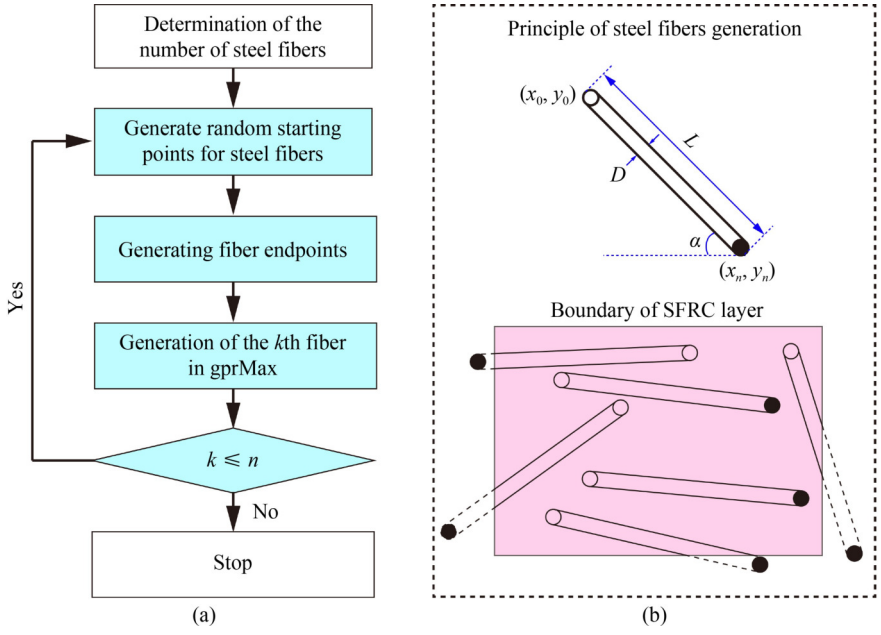

Fig. 5 The generation method for steel fibers in the SFRC layer: (a) the process of the generation; (b) the principle of the generation and the main parameters of steel fibers.

3.2.2.2 Grout thickness distribution

In addition, the model considered the uneven grouting body to simulate the randomness of grout distribution in actual projects. The statistical results of the distribution of grout thickness are shown in Fig. 7, which is distributed between 0.05 and 0.16 m, with mean and median values of 0.116 m and 0.107, respectively. The range of grout thickness distribution in the model is representative of different thicknesses in real projects. At the back of the grouting body, there is a rock/soil layer.

3.2.2.3 Material parameters

In the SFRC-RC composite lining, electrical parameters, including relative dielectric constant, conductivity, and relative magnetic permeability, have a significant impact on the propagation of GPR waves. The medium parameters of the numerical model are shown in Table 2. Specifically, since all materials used in the study are non-magnetic or irrelevant to magnetism, the relative magnetic permeability of all materials was set to 1. The "free_space" material in gprMax was used to simulate voids [43], and the "pec" material was used to simulate steel fibers [44,45].

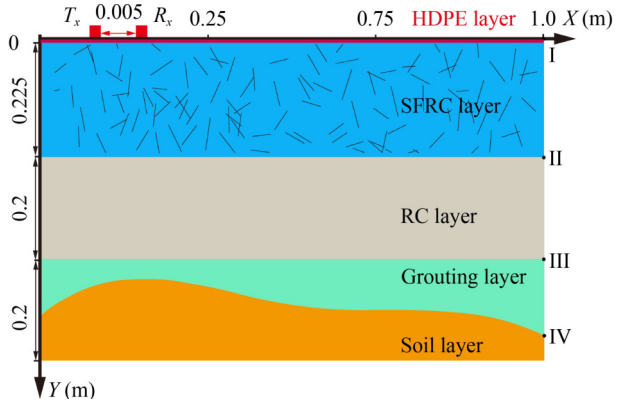

Fig. 6 gprMax numerical model for SFRC-RC composite lining.

3.2.3 Parameters for ground penetrating radar detection

As displayed in Fig. 6, we selected the Hertzian dipole model in gprMax to simulate the GPR antenna, with a fixed antenna spacing of 0.005 m in the detection process. The starting point of the monitoring line is located at the lower-left corner of the numerical model, and the GPR antenna moves with a step size of 0.005 m. Regarding the GPR data acquisition parameters, each survey line collects data from 147 monitoring points, and the sampling time window is set to 40 ns.

Existing research outcomes [28] demonstrated that in comparison to frequencies of 200 and 1000 MHz, GPR at 500 MHz exhibits superior penetration capability for SFRC segments. While the focus of this study is on SFRC-RC composite lining rather than pure SFRC segments, their outcomes still offered valuable insights that can inform the frequency selection in our study. Hence, frequencies of 300, 400, 600, and 700 MHz, chosen for their proximity to the 500 MHz frequency, were individually employed in numerical simulations of the identical model. This was undertaken to explore the efficacy of detecting SFRC-RC composite lining at varying frequencies, as well as to probe the response characteristics of diverse GPR frequencies to dissimilar material interfaces.

3.3 Numerical analysis at various ground penetrating radar frequencies

The B-scans at four different GPR frequencies are shown in Fig. 8, and it can be observed from the figure that GPR exhibits significant variations in its detection capabilities for the interface of the SFRC-RC composite lining at different probing frequencies. The specific characteristics are as follows.

1) The results at 300 and 400 MHz are similar, as depicted in Figs. 8(a) and 8(b). Both frequencies exhibit more pronounced detection effects on interfaces I, III, and IV, while the detection effect on interface II is not significant.

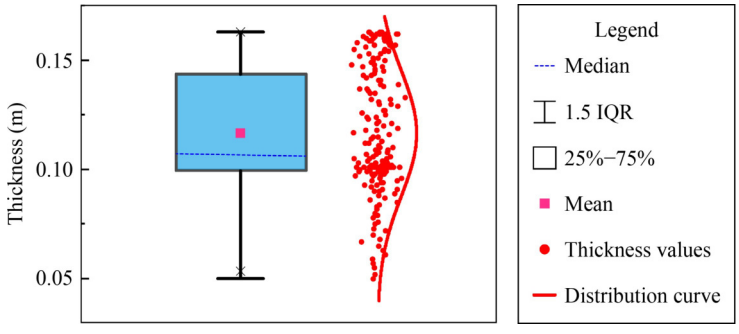

Fig. 7 The distribution of grout thickness in the gprMax numerical model. Note: the IQR represents the Interquartile Range, which is the difference between the first quartile (Q1) and the third quartile (Q3) and is often used to identify outliers and the stability of data distribution.

2) As shown in Figs. 8(c) and 8(d), the numerical results at 600 and 700 MHz are quite similar as well. They exhibit relatively clear resolution for interfaces I and II, but their ability to reflect deeper interfaces III and IV is limited, with visibility only in localized regions.

3) Steel fibers exhibit a more complex wave reflection in the B-scans. Regarding the characterization of steel fiber reflection in GPR imaging, it can be analyzed that the sensitivity of 300 and 400 MHz to steel fiber reflections is lower compared to 600 and 700 MHz.

Due to the identical material parameters of concrete in the numerical model for both the SFRC layer and the RC layer, and considering the random distribution of steel fibers within the SFRC layer, the interfaces between the SFRC layer and the RC layer are not perfectly straight and regular. This non-uniformity in the interface geometry leads to a nonlinear distribution of the reflective surface in the B-scans. In Figs. 8(c) and 8(d), the criterion for identifying interface II is based on the presence of significant steel fiber reflections within the SFRC layer, while there are no such reflections within the RC layer.

In summary, compared to 600 and 700 MHz, 300 and 400 MHz exhibit stronger detection capabilities for deeper interfaces such as III and IV, whereas the 600 and 700 MHz provide a better response to the characteristics of the SFRC layer. In practical engineering applications, the SFRC layer and RC are artificially prefabricated with more controllable quality, while there is greater uncertainty in the quality of the grouting layer. Therefore, when conducting quality assessments of the grouting layer, it is advisable to choose lower-frequency GPR.

Table 2 Material parameter of the numerical model

Material	Relative dielectric constant	Conductivity ($S \cdot m^{-1}$)
Concrete	9	0.005
Rock/Soil	5	0.005
HDPE	7	0.005
Grouting materials	25	0.008
Steel fibers/pec	∞	∞
Air/free_space	1	0

4 Model experiments and field testing

4.1 Engineering background

The DTSS is a superhighway for Singapore's used water management, which conveys used water entirely by gravity to three centralized treatment plants strategically located in coastal areas [46]. The project is divided into Phase 1 and Phase 2, and this paper mainly focuses on Phase 2. Phase 2 covers the western part of the country with an additional 100 km of sewers that would end at the Tuas Water Reclamation Plant. The Phase 2 consists of 40 km of deep tunnels with internal diameters of 3–6 m and 10 km of the larger diameter Link Sewers, which are both constructed using a shield tunnelling method.

Taking the Southern Region Link Sewer Tunnel as an example, the geology where the tunnel passes is predominantly as follows. 1) Sedimentary rocks and soils of the Jurong Formation; 2) completely and highly weathered rocks which are highly undulating and variable due to faulting and folding. The main geotechnical risks of tunnel boring are tunneling in the mixed face, water ingress, ground settlement, and tunneling below the sea, which imposes high requirements on the lining support of

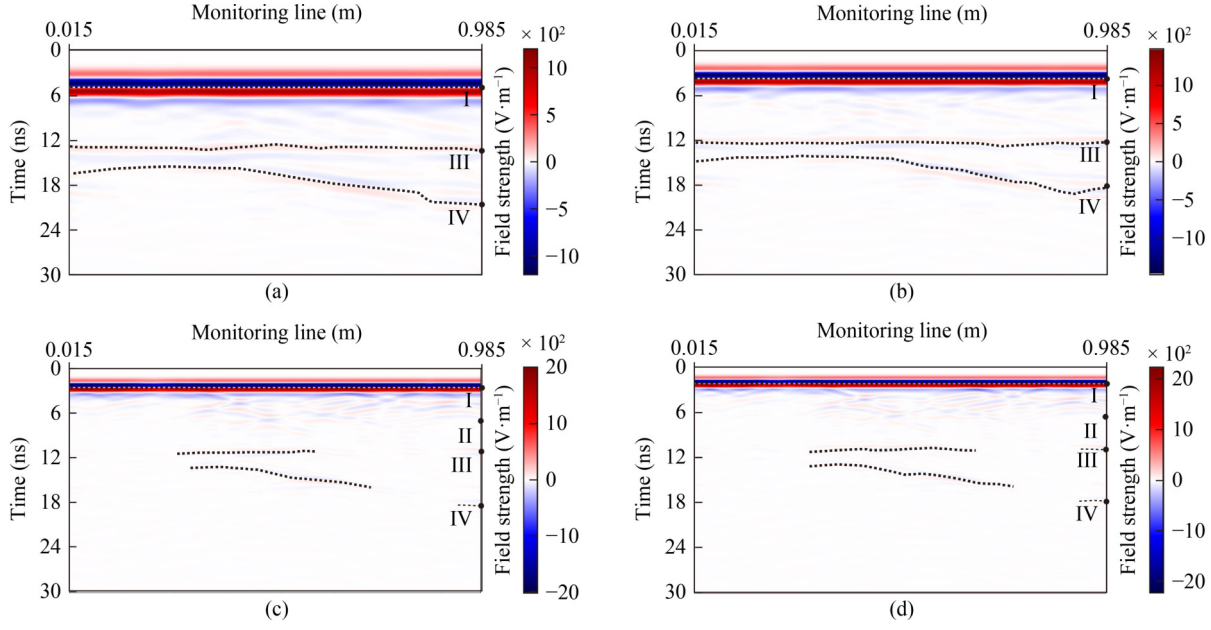

Fig. 8 B-scans from numerical simulations at various GPR frequencies: (a) 300 MHz; (b) 400 MHz; (c) 600 MHz; (d) 700 MHz.

the tunnel. To ensure the tunnel lining possesses excellent mechanical and impermeable properties, this project adopts a composite lining structure composed of a waterproof layer, an SFRC layer, and an RC layer.

4.2 Ground penetrating radar equipment

4.2.1 Ground penetrating radar hardware and parameter settings

The GPR used for this study is a dual-channel antenna, meaning each antenna has two different frequencies. The frequency combinations of the two antennas are 300/700 MHz and 400/600 MHz, respectively. The main parameters of the two GPR antennas are displayed in Table 3. The composition of the dual-channel antenna allows for a more compact hardware structure, making the detection more efficient. The GPR does not have a main unit but instead transfers data directly to a computer through an Ethernet cable. During the detection process, it can be triggered through a measuring wheel to assist in accurately recording the detection distance.

4.2.2 Time–frequency characteristics of source wave

The time–frequency characteristics of GPR have a significant impact on its performance. The time–frequency spectra of two types of GPR antennas with frequencies used in this study are shown in Fig. 9. As can be seen from the figures, The four frequencies, 300 and 400 MHz are not specific values but rather distributed within certain frequency bands. The frequency band of the GPR raw waveforms increases with the increase in frequency. The frequency band around 300 MHz is more concentrated, while the frequency range around 700 MHz is the widest. However, the position of the maximum intensity of the frequency of these frequencies, matches well with the nominal frequencies and demonstrates the good time–frequency characteristics of the GPR device itself.

Table 3 The main parameters of dual-frequency antennas

Parameter	Value
Channels	2
Minimum resolution (ps)	1
Time window	0 ns–2.5 μs
Voltage (V)	9–18
Working temperature (°C)	−30–50

4.3 Testing scheme

The testing is mainly divided into two parts: a full-scale model experiment and the field test, as shown in Fig. 10. The full-scale model was artificially prefabricated in advance, its structure and quality are known, which can help me better eliminate factors other than the experimental variables. Meanwhile, the field test of the tunnel ensures a more realistic detection scenario, guaranteeing that the detection results are more representative and convincing. The specific details of these two schemes are as follows.

4.3.1 Full-scale model experiment

As shown in Fig. 10(a), the lining structure of the model experiment is the same as the tunnel design, but it lacks the grouting layer on the outside. The GPR detection line was located on the inner side of the model, with a length of 1.2 m. The steel plate brackets on the outside of the lining can act as strong reflectors, helping us assess the penetration performance of the GPR. When strong reflectors exhibit distinct characteristics in GPR waveforms, it demonstrates that the GPR waves at the

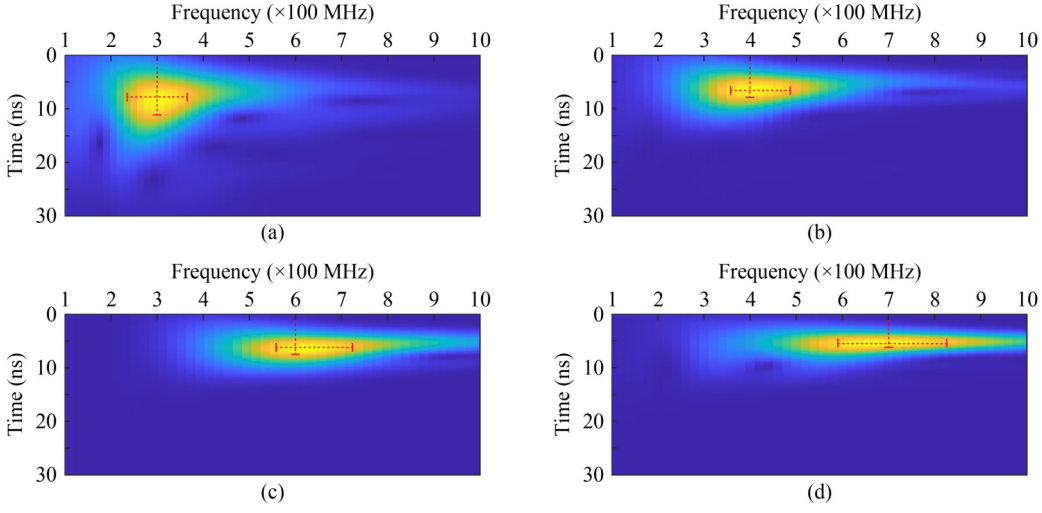

Fig. 9 The time–frequency spectra of the GPR source wave: (a) 300 MHz; (b) 400 MHz; (c) 600 MHz; (d) 700 MHz.

corresponding frequency possess favorable penetration capabilities through the SFRC-RC composite lining.

To study the penetrability of the selected frequencies through the SFRC-RC composite lining, we opted for the lowest and highest frequencies among the four, namely 300 and 700 MHz, to conduct line scans and assess their imaging effects.

4.3.2 Field testing for deep tunnel sewerage system phase 2

The monitoring line for the field test inside the tunnel, as shown in Fig. 10(b), has a length of 5.6 m, and two antennas with four frequencies were employed to detect the same line. The monitoring line was located in the lower right corner of the tunnel, distributed along the tunnel's direction to ensure that the detection range covers more rings, thus reducing the random errors introduced by single-ring construction.

The GPR acquisition parameters were the same for both the model experiment and the field test. The time window was set to 40 ns; the sampling interval was 0.5 cm per trace, meaning that each monitoring line collected 1119 A-scans; and the number of waveform stacking was set to 16. Moreover, due to the different propagation speeds of electromagnetic waves at different frequencies in the medium, there are significant differences in the temporal characteristics of their waveforms. To better reflect the detection characteristics at different frequencies, necessary data trimming and processing are essential.

4.4 Model experiment data analysis

The B-scans of the model experiment under 300 and 700 MHz are presented in Figs. 11(a) and 11(b), respectively. In the B-scan of 300 MHz, significant co-phased axes were observed at 4, 5, 10, and 16 ns, indicating the presence of interfaces in these locations. These interfaces are tentatively identified as the boundaries of mediums I, II, III, and IV, respectively. Within the range of 0.8 to 1 m, the signal intensity of GPR shows a significant enhancement, and multiple strong reflections are present in the time domain beyond 16. This indicates that the signal enhancement is caused by strong reflections from the steel plate behind the model. Along the monitoring line, except for the range of 0.8 to 1 m, the co-phased axes in other parts are consistently straight and uniform. This indicates that the thickness of each layer is stable, suggesting the absence of voids or debonding within the lining. This confirms the good quality of the prefabricated model.

As shown in Fig. 11(b), the B-scan of 700 MHz shows significant differences compared to the 300 MHz. It cannot display the complete interfaces of the composite lining like the 300 MHz B-scan, and can only exhibit the interfaces of shallow layers. It can still capture the strong reflection characteristics of the steel plate and is aligned with the survey positions under 300 MHz. However, the reflection features of the steel plate with the 700 MHz GPR wave are not as pronounced as those observed with the 300 MHz wave.

The model experiment results indicate that the 300 MHz frequency demonstrates more significant penetration capability and detection effectiveness of the interfaces in the SFRC-RC composite lining, compared to 700 MHz. This is because the 700 MHz GPR waves experience more significant attenuation within the composite lining, making it unable to image the interfaces at deeper layers.

4.5 Analysis of field test data

4.5.1 Analysis of A-scan characteristics

The representative A-scans of the field GPR data in the DTSS Phase 2 tunnel can display different waveform characteristics at specific monitoring points. As

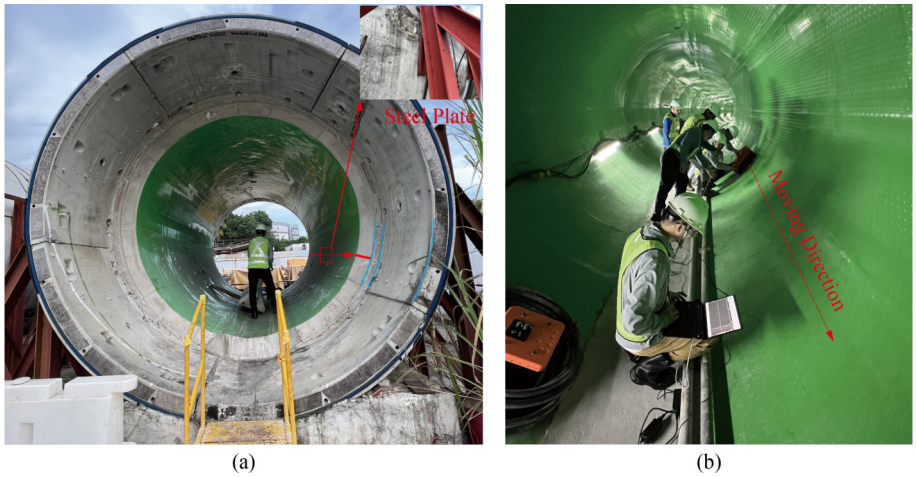

(a) (b)

Fig. 10 GPR detection testing: (a) model experiment; (b) tunnel field testing.

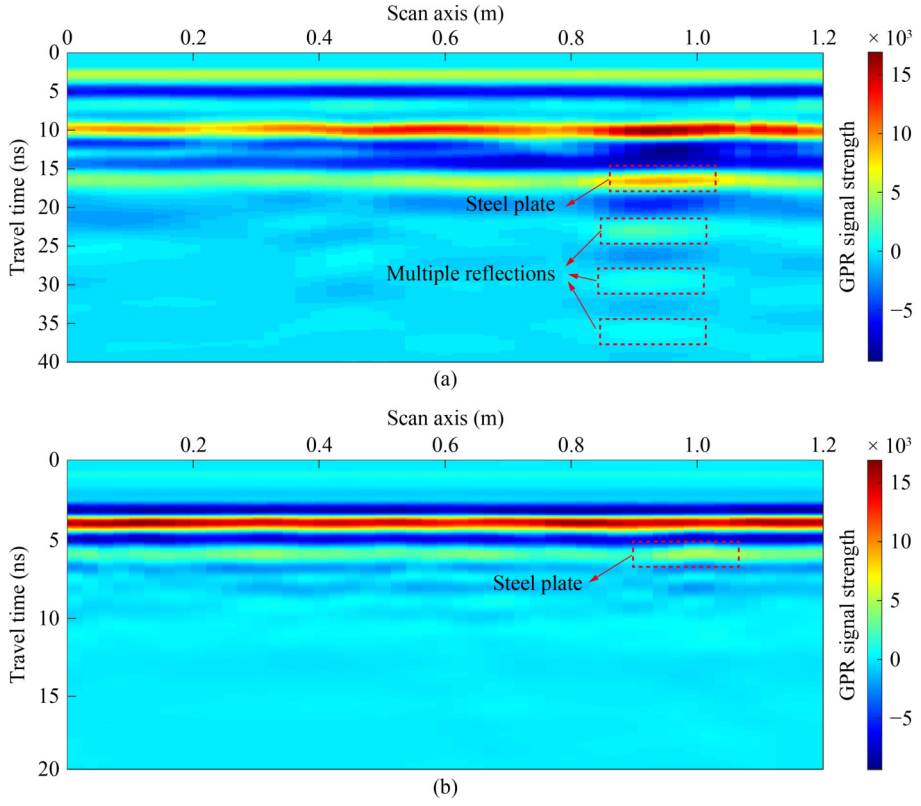

Fig. 11 GPR results: (a) 300 MHz; (b) 700 MHz.

illustrated in Fig. 12, the A-scan at the 500th monitoring point was randomly selected for analysis at four different frequencies. The 300 MHz A-scan exhibits significant amplitude fluctuations around 5, 10, 15, and 20 ns, representing the interfaces of I–IV. Within the range of 5 to 10 ns, the waveform transition is relatively smooth, and there are no strong reflections or multiple reflection characteristics from the steel fibers in the waveform. As shown in Figs. 12(b)–12(d), the A-scans at 400, 600, and 700 MHz can partially display some interfaces to varying

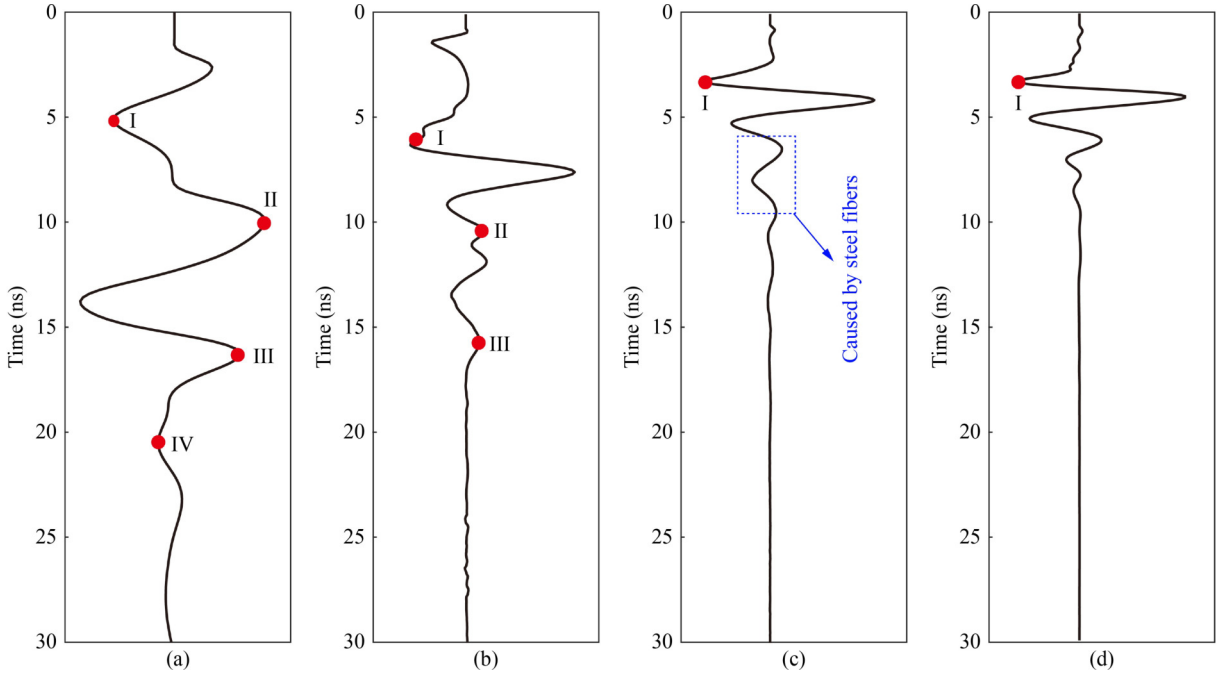

Fig. 12 A-scans of field test for GPR frequencies: (a) 300 MHz; (b) 400 MHz; (c) 600 MHz; (d) 700 MHz. Note: The red dots in the figure indicate manual annotations based on the GPR waveform.

degrees, but none of them can present the waveform characteristics of all material interfaces like 300 MHz. The waveforms of displayed interfaces gradually decrease, but higher frequencies make the waveform characteristics of shallow steel fibers more pronounced as the frequency increases.

4.5.2 Power characteristics of ground penetrating radar waves in steel fiber reinforced concrete-reinforced concrete composite lining

4.5.2.1 Analysis of the characteristics of instantaneous power attenuation

The propagation of GPR signals within a medium is accompanied by attenuation, and the varying degrees of attenuation significantly influence the detectability of targets and the quality of imaging. The mean and median of instantaneous power attenuation of GPR signals at four frequencies are shown in Fig. 13. These are depicted by the green dotted line and the bold black solid line, respectively. The characteristics of power attenuation were analyzed as follows.

1) When analyzing the instantaneous GPR power attenuation, the median and mean can offer distinct information about data distribution and trends. The median is better suited for situations where there are outliers or anomalies within the data, while the mean is more effective at illustrating the overall average level. The mean and median values at the four GPR frequencies exhibit a notable level of overlap, indicating a relatively consistent pattern of energy attenuation and a limited presence of extreme values.

2) In terms of the general trends, the GPR energy within the SFRC-RC composite lining primarily follows an attenuation pattern. The attenuation of GPR signals at 300 MHz demonstrates consistent stability, with a relatively modest degree of signal loss. GPR waveforms at higher frequencies experience greater interference within the SFRC-RC composite lining.

3) The GPR signals at the three frequencies other than 300 MHz experience a sharp attenuation within the 5–20 ns range. This time range corresponds to the composite lining layer as shown in Fig. 14(a). However, within the range of 20 to 30 ns, the GPR signal at 300 MHz continues to exhibit a gradual attenuation at a relatively

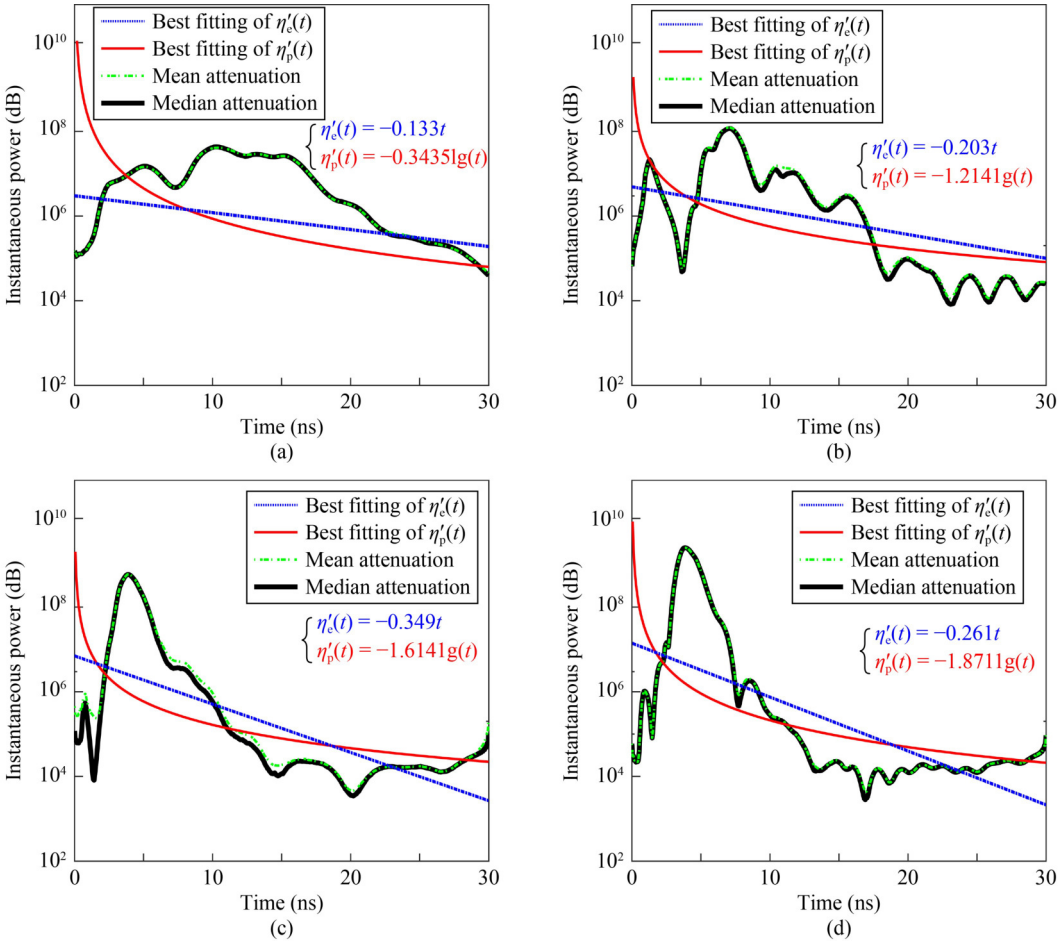

Fig. 13 Instantaneous power attenuation patterns of GPR signals in SFRC-RC composite lining at various frequencies: (a) 300 MHz; (b) 400 MHz; (c) 600 MHz; (d) 700 MHz.

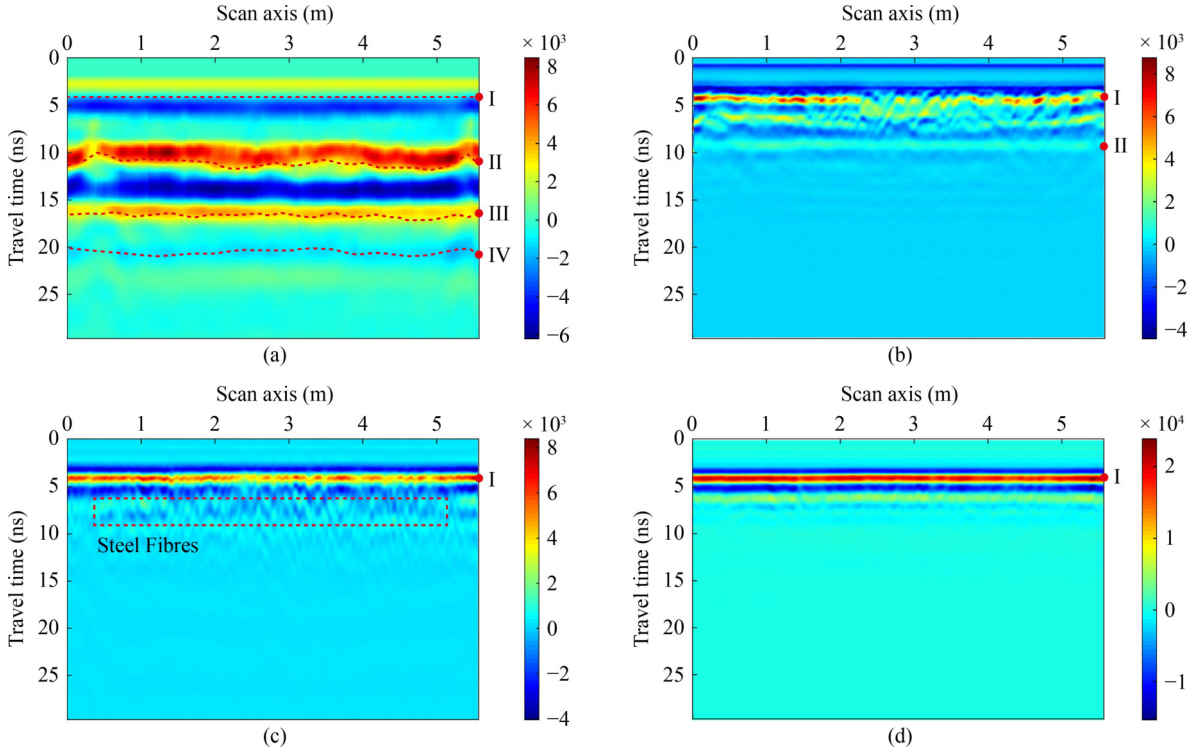

Fig. 14 B-scans of field test under four GPR frequencies: (a) 300 MHz; (b) 400 MHz; (c) 600 MHz; (d) 700 MHz. Note: The red dots and dashed lines in the figure indicate manual annotations based on the GPR waveform.

low rate. On the other hand, the signal at 400 MHz approaches nearly no attenuation (the curve levels off). Meanwhile, at 600 and 700 MHz, there is an observed phenomenon of gradual power increase.

4) The manual operation of the GPR device during detection can introduce instability in data collection, potentially leading to variations in the power attenuation patterns of electromagnetic waves across the four GPR frequencies. For example, a sudden drop in power attenuation may occur at 5 ns in the 400 MHz frequency (as shown in Fig. 13(b)). Moreover, this instability can potentially be mitigated through the adoption of more stable data collection methods.

Based on the aforementioned analysis, it can be concluded that, in the case of field-tested GPR data, the attenuation is relatively stable but lacks a clear pattern. As a result, the analysis of such data often allows only for qualitative assessments.

4.5.2.2 Empirical function of instantaneous power attenuation

To achieve a more profound understanding and quantitative assessment of the attenuation patterns, we conducted separate exponential and power function fittings combining the attenuation patterns shown in these figures. The instantaneous power, denoted as η, corresponds to a specific time value t on the GPR A-scan. The equations for the two types of fitting are presented in Eq. (5):

$$\begin{cases} \eta_{\mathrm{e}}(t) = \mathrm{e}^{-k_1 t}, \\ \eta_{\mathrm{p}}(t) = t^{-k_2}, \end{cases} \tag{5}$$

where $\eta_{\mathrm{e}}(t)$ and $\eta_{\mathrm{p}}(t)$ represent the fitting function of the exponential fitting and power fittings; e is a commonly used irrational number, with a value of 2.71828; k_1 and k_2 are the fitting coefficients of two fitting methods.

For a clearer representation of coefficients and patterns in the figure, we conducted natural logarithm and logarithmic transformations on $\eta_{\mathrm{e}}(t)$ and $\eta_{\mathrm{p}}(t)$, respectively. As a result, Eq. (5) becomes Eq. (6):

$$\begin{cases} \eta'_{\mathrm{e}}(t) = -k_1 t, \\ \eta'_{\mathrm{p}}(t) = -k_2 \lg(t), \end{cases} \tag{6}$$

where $\eta'_{\mathrm{e}}(t)$ and $\eta'_{\mathrm{p}}(t)$ represent the transformed fitting functions of $\eta_{\mathrm{e}}(t)$ and $\eta_{\mathrm{p}}(t)$.

The best fitting curve of $\eta'_{\mathrm{e}}(t)$ and $\eta'_{\mathrm{p}}(t)$ at four frequencies of 300, 400, 600, and 700 MHz within the SFRC-RC composite lining are depicted by the blue dashed line and the red solid line in Fig. 13. It is evident that both $\eta'_{\mathrm{e}}(t)$ and $\eta'_{\mathrm{p}}(t)$ are decreasing functions of their independent variable t. By comparing the magnitudes of the k_1 and k_2 in the fitting functions at different frequencies, the extent of attenuation in GPR signals can be directly determined to some extent. The values of k_1 and k_2 at four different frequencies, along with their corresponding empirical equations, are shown in Table 4. As shown in the table, apart from the 700 MHz data in $\eta_{\mathrm{p}}(t)$, it is evident that the power attenuation of GPR

within the SFRC-RC lining generally follows an increasing trend with higher frequencies. The gradual increase in energy attenuation between 20 to 30 ns has led to a reduction in the value of k_1 in the $\eta_e(t)$ at 700 MHz. Under the same conditions, the $\eta_p(t)$ cannot represent this relationship. These results indicate that the $\eta_e(t)$ function provides a more precise characterization of energy attenuation.

Table 4 Fitting coefficients of power attenuation at different frequencies

Fitting coefficient	GPR frequency (MHz)			
	300	400	600	700
k_1	0.133	0.203	0.349	0.261
k_2	0.344	1.214	1.614	1.871

4.5.3 B-scans at different ground penetrating radar frequencies

The B-scans of the field test under GPR frequencies are shown in Fig. 14. As shown in Fig. 14(a), the results at 300 MHz exhibit a good representation of the interfaces between each layer of the medium. The positions of the interfaces I, II, III, and IV are approximately 5, 11, 16, and 20 ns, respectively. The co-phase axis of each layer is significant and continuous. However, B-scans at the other three frequencies are unable to comprehensively represent all interfaces within the SFRC-RC composite lining. Moreover, as the frequency increases, the display depth of material interfaces becomes more restricted. Figure 14(b) can only display interfaces I and II, while Figs. 14(c) and 14(d) can only display interface I. The frequencies of 400 and 600 MHz demonstrate good capabilities in capturing multiple reflections caused by the steel fibers, with 600 MHz exhibiting even stronger capabilities in visualizing the steel fibers than 400 MHz. The GPR signal at 700 MHz only exhibits higher intensity in the surface layer of the SFRC-RC composite lining. However, its ability to detect steel fiber features and deeper interfaces is relatively weak.

The results of the model experiment all indicate that the 300 MHz GPR has a better detection capability for the medium interfaces of the SFRC-RC composite lining. It also serves as validation for the numerical simulation results.

5 Discussion

Compared with traditional RC segmental linings, SFRC-RC composite linings exhibit favorable mechanical strength and impermeability in engineering projects such as shield tunnels. In this paper, our primary focus is on the GPR detection of SFRC-RC composite tunnel lining. We investigated the potential application of GPR in quality assessment within this field and researched suitable detection frequencies and signal attenuation patterns.

There is limited research on GPR detection of SFRC-RC composite segments. Hence, when it came to selecting GPR frequencies, we looked to studies involving the penetration capabilities of pure SFRC segments. Consequently, we opted for frequencies of 300, 400, 600, and 700 MHz, which are near the 500 MHz range. The research results indicate that lower GPR frequencies, such as 300 MHz, offer better delineation imaging of the interfaces within SFRC-RC composite lining. In addition, this study primarily focuses on the penetration performance of GPR on the novel composite lining and does not aim to study the precise determination of interface positions. As a result, the numerical simulations and field testing conditions were relatively simple, leading to correspondingly straightforward waveform characteristics in the detection results. Therefore, the experimental and field data in this study underwent only basic filtering and gain adjustments, without further exploration of advanced data analysis methods. In future research, we anticipate developing data processing methods specifically tailored for composite linings and their associated GPR detection frequencies. This advancement is expected to significantly enhance the detection efficacy of GPR in these tunnel structures.

The HDPE layer is non-metallic and non-magnetic, and its thickness is relatively thin. We speculate that the propagation of GPR in it is essentially unaffected. Therefore, it was not analyzed as a separate layer. While this layer was included in the numerical model, it was not considered a primary focus of our study.

In terms of GPR power attenuation analysis, we can achieve a relatively sound qualitative understanding of energy decay through the patterns of mean and median distribution. However, this understanding cannot be subjected to quantitative analysis and comparison. The exponential and power function fittings we opted for are based on the intrinsic characteristics of the attenuation law itself. By considering the behavior of the functions and the fitting coefficients, we can effectively characterize the degree of attenuation at various frequencies. This approach offers a robust quantitative representation method. We opted for relatively simple function models, such as $\eta_e(t)$ and $\eta_p(t)$, to maintain single coefficients in the empirical equations for fitting. This approach aims to minimize interference in characterizing the attenuation characteristics of GPR signals.

6 Conclusions

This paper takes the DTSS Phase 2 in Singapore as an

engineering background to investigate the potential of GPR for quality detection in SFRC-RC composite lining of shield tunnels. Numerical simulations, model experiments, and field engineering tests were carried out to study the GPR waveforms, imaging characteristics, and power attenuation patterns in SFRC-RC lining. Through these studies, this paper proposed the optimal detection frequency for SFRC-RC composite lining and also presented an empirical formula for power attenuation of GPR signals in SFRC-RC composite lining. The specific research conclusions are as follows.

1) A gprMax numerical model, incorporating actual steel fiber parameters, was established for the SFRC-RC composite lining. Numerical simulations indicate that 300 and 400 MHz exhibit superior detection capabilities for deeper interfaces such as III and IV.

2) Based on the analysis of GPR signal attenuation patterns in SFRC-RC composite lining at frequencies of 300, 400, 600, and 700 MHz, the attenuation empirical equations were fitting. This enables a quantitative characterization of different attenuation situations through the fitting coefficients of empirical equations. The exponential function model $\eta_e(t)$ effectively reflects the attenuation characteristics of the four frequencies within the SFRC-RC composite lining. The attenuation coefficients corresponding to 300, 400, 600, and 700 MHz are 0.133, 0.203, 0.349, and 0.261, respectively.

3) GPR was validated as an effective means of non-destructive testing of SFRC-RC composite linings. After selecting and comparing four different frequencies (300, 400, 600, and 700 MHz), it was determined that 300 MHz is the optimal frequency for detecting the interfaces of SFRC-RC composite lining.

Acknowledgements This work was supported by the National Key R&D Program of China (No. 2023YFC3806705), the National Natural Science Foundation of China (Grant Nos. 52038008 and 52378408), the Science and Technology Innovation Plan of Shanghai Science and Technology Commission (No. 22dz1203004), and the Science and Technology Project of State Grid Corporation of China (No. 5200-202417104A-1-1-ZN).

Competing interests The authors declare that they have no competing interests.

References

1. Guo W, Feng K, Lu X, Qi M, Liu X, Fang Y, He C, Xiao M. Model test investigation on the longitudinal mechanical property of shield tunnels considering internal structure. Tunnelling and Underground Space Technology, 2023, 140: 105293
2. Li C, Zhang W, Wang X, Pan B, Zhu H, Spencer B F. Modeling dynamic responses of a cross-river road shield tunnel under stochastic vehicle loads. Tunnelling and Underground Space Technology, 2020, 102: 103432
3. Jiang X, Zhang Y, Zhang Z, Bai Y. Study on risks and countermeasures of shallow biogas during construction of metro tunnels by shield boring machine. Transportation Research Record: Journal of the Transportation Research Board, 2021, 2675(7): 105–116
4. Su E, Zhang X, Wen X, Liu J, Ye F, Han X, Lei P. Visual characteristics of drivers in different directions and lengths of gradual landscape zones in extra-long highway tunnels. Tunnelling and Underground Space Technology, 2023, 137: 105136
5. Guo Y, Wang Y, Geng F, Zhang Z. Study on dust distribution in a highway tunnel during the full-face excavation with Drilling-Blasting method. Tunnelling and Underground Space Technology, 2023, 139: 105229
6. Lu B, Zhao W, Wang W, Jia P, Du X, Cao W, Li W. Design and optimization of secant pipe roofing structure applied in subway stations. Tunnelling and Underground Space Technology, 2023, 135: 105026
7. Yang B, Sun Y, Yao Y, Ni L. Field measurement and analysis of subway tunnel thermal environment in severe cold region. Building and Environment, 2023, 243: 110629
8. Wan L, Xie X, Wang L, Li P, Huang Q. Modal analysis of subway tunnel in soft soil during operation. Underground Space, 2023, 8: 181–195
9. Zhao D, Huang Y, Chen X, Han K, Chen C, Zhao X, Chen W. Numerical investigations on dynamic responses of subway segmental tunnel lining structures under internal blasts. Tunnelling and Underground Space Technology, 2023, 135: 105058
10. Khanlari G, Ghaderi Meybodi R, Mokhtari E. Engineering geological study of the second part of water supply Karaj to Tehran tunnel with emphasis on squeezing problems. Engineering Geology, 2012, 145–146: 9–17
11. Wang X F, Zhou X J, Hu H Y. Study on selection of the length of reinforced concrete segment for oil and gas shield tunnel with 3D numerical analysis. Applied Mechanics and Materials, 2014, 488–489: 517–520
12. Zhang X P, Tang S H, Liu Q S, Wang H J, Li X F, Chen P, Liu H. Key technology for the construction and inspection of long-distance underwater tunnel for 1000 kV gas-insulated transmission line. Bulletin of Engineering Geology and the Environment, 2023, 82(1): 7
13. Barla M, Insana A. Energy tunnels as an opportunity for sustainable development of urban areas. Tunnelling and Underground Space Technology, 2023, 132: 104902
14. He S, Lai J, Wang L, Wang K. A literature review on properties and applications of grouts for shield tunnel. Construction and Building Materials, 2020, 239: 117782
15. Ye X W, Jin T, Chen Y M. Machine learning-based forecasting of soil settlement induced by shield tunneling construction. Tunnelling and Underground Space Technology, 2022, 124: 104452
16. Ding W, Duan C, Zhu Y, Zhao T, Huang D, Li P. The behavior of synchronous grouting in a quasi-rectangular shield tunnel based on a large visualized model test. Tunnelling and Underground Space Technology, 2019, 83: 409–424
17. Xu J, Ding L, Luo H, Chen E J, Wei L. Near real-time circular tunnel shield segment assembly quality inspection using point cloud data: A case study. Tunnelling and Underground Space

Technology, 2019, 91: 102998
18. Shi Z, Xie X, Zeng H, Zeng K, Niu G, Xiao Z. Disaster mechanism of large-diameter shield tunnel segments under multi-source load coupling: A case study. Engineering Failure Analysis, 2024, 166: 108878
19. Yang K, Yan Q, Zhang C. Three-dimensional mesoscale numerical study on the mechanical behaviors of SFRC tunnel lining segments. Tunnelling and Underground Space Technology, 2021, 113: 103982
20. Oliveira J M J, Vieira C S, Silva M F A, Amorim D L N F. Fracture modelling of steel fibre reinforced concrete structures by the lumped damage mechanics: Application in precast tunnel segments. Engineering Structures, 2023, 278: 115487
21. Bentur A, Mindess S. Fibre Reinforced Cementitious Composites. London: Chemical Rubber Company Press, 2006
22. Caratelli A, Meda A, Rinaldi Z. Design according to MC2010 of a fibre-reinforced concrete tunnel in Monte Lirio, Panama. Structural Concrete, 2012, 13(3): 166–173
23. Peng M, Wang D, Liu L, Shi Z, Shen J, Ma F. Recent advances in the GPR detection of grouting defects behind shield tunnel segments. Remote Sensing, 2021, 13(22): 4596
24. Liu H, Yue Y, Lai S, Meng X, Du Y, Cui J, Spencer B F. Evaluation of the antenna parameters for inspection of hidden defects behind a reinforced shield tunnel using GPR. Tunnelling and Underground Space Technology, 2023, 140: 105265
25. Xiang L, Zhou H L, Shu Z, Tan S H, Liang G Q, Zhu J. GPR evaluation of the Damaoshan highway tunnel: A case study. Non-Destructive Testing and Evaluation International, 2013, 59: 68–76
26. Qin H, Tang Y, Wang Z, Xie X, Zhang D. Shield tunnel grouting layer estimation using sliding window probabilistic inversion of GPR data. Tunnelling and Underground Space Technology, 2021, 112: 103913
27. Han W, Jiang Y, Wang G, Liu C, Koga D, Luan H. Review of health inspection and reinforcement design for typical tunnel quality defects of voids and insufficient lining thickness. Tunnelling and Underground Space Technology, 2023, 137: 105110
28. Li K, Xie X, Huang C, Zhou B, Duan W, Lin H, Wang C. Study on the penetration capability of GPR for the steel-fibre reinforced concrete (SFRC) segment based on numerical simulations and model test. Construction and Building Materials, 2023, 400: 132719
29. Manhães P M B, Júnior J T A, Chen G, Anderson N L, Pereira E V, de Andrade Silva F. The use of GPR to investigate the effect of steel fiber distribution on the mechanical behavior of FRC. Construction and Building Materials, 2022, 344: 128248
30. Jol H M. Ground Penetrating Radar Theory and Applications. Amsterdam: Elsevier, 2008
31. Wee J W, Chudnovsky A, Choi B H. Crack layer modeling of overload-induced slow crack growth retardation of high-density polyethylene. International Journal of Mechanical Sciences, 2023, 257: 108546
32. Ezazi M, Hossaini M F, Sheikhmali R, Khosrotash M, Sharifi Teshnizi E, O'Kelly B C. Assessment of steel-fiber reinforced segmental lining of Chamshir water conveyance tunnel, Iran: Integrating laboratory experiments, field observations, and numerical analysis. Case Studies in Construction Materials, 2024, 20: e03144
33. Maxwell J C. VIII. A dynamical theory of the electromagnetic field. Philosophical Transactions of the Royal Society of London, 1865, 155: 459–512
34. Giannopoulos A. Modelling ground penetrating radar by gprMax. Construction and Building Materials, 2005, 19(10): 755–762
35. Warren C, Giannopoulos A, Giannakis I. gprMax: Open source software to simulate electromagnetic wave propagation for Ground Penetrating Radar. Computer Physics Communications, 2016, 209: 163–170
36. Giannakis I, Giannopoulos A, Warren C. A realistic FDTD numerical modeling framework of ground penetrating radar for landmine detection. IEEE Journal of Selected Topics in Applied Earth Observations and Remote Sensing, 2015, 9(1): 37–51
37. Warren C, Giannopoulos A. Creating finite-difference time-domain models of commercial ground-penetrating radar antennas using Taguchi's optimization method. Geophysics, 2011, 76(2): G37–G47
38. Yee K S. Numerical solution of initial boundary value problems involving Maxwell's equations in isotropic media. IEEE Transactions on Antennas and Propagation, 1966, 14(3): 302–307
39. Giannopoulos A. Unsplit implementation of higher order PMLs. IEEE Transactions on Antennas and Propagation, 2012, 60(3): 1479–1485
40. Li C, Cai L, Guo L, Chen D. Research on target recognition method of tunnel lining image based on deep learning. In: 2022 IEEE 6th Information Technology and Mechatronics Engineering Conference (ITOEC). Chongqing: IEEE, 2022, 6: 1833–1837
41. Qin H, Zhang D, Tang Y, Wang Y. Automatic recognition of tunnel lining elements from GPR images using deep convolutional networks with data augmentation. Automation in Construction, 2021, 130: 103830
42. Go G H, Lee S J. A Study on numerical analysis for GPR signal characterization of tunnel lining cavities. Journal of the Korean Geotechnical Society, 2021, 37(10): 65–76
43. Giannopoulos A, Warren C. gprMax: Electromagnetic simulation software. 2025 (available at the website of gprMax)
44. Ponti F, Barbuto F, di Gregorio P P, Mangini F, Simeoni P, Troiano M. Deep learning for applications to ground penetrating radar and electromagnetic diagnostic. In: 2019 Photonlcs and Electromagnetics Research Symposium-Spring (PIERS-Spring). Rome: IEEE, 2019: 547–551
45. Dogan M, Turhan-Sayan G. Investigation of the effects of buried object orientation in subsurface target detection by GPR. In: 2017 7th IEEE International Symposium on Microwave, Antenna, Propagation, and EMC Technologies (MAPE). Xi'an: IEEE, 2017: 475–479
46. Singapore's National Water Agency. Deep Tunnel Sewerage System (DTSS). 2023